JACS
JOURNAL OF THE AMERICAN CHEMICAL SOCIETY
Communication
pubs.acs.org/JACS

Correlation of π-Conjugated Oligomer Structure with Film Morphology and Organic Solar Cell Performance

Roland Fitzner,[†] Elena Mena-Osteritz,[†] Amaresh Mishra,[†] Gisela Schulz,[†] Egon Reinold,[†] Matthias Weil,[‡] Christian Körner,[∥] Hannah Ziehlke,[∥] Chris Elschner,[∥] Karl Leo,[∥] Moritz Riede,[∥] Martin Pfeiffer,[§] Christian Uhrich,[§] and Peter Bäuerle*,[†]

[†]Institut für Organische Chemie II und Neue Materialien, Universität Ulm, Albert-Einstein-Allee 11, 89081 Ulm, Germany

[‡]Institut für Chemische Technologien und Analytik, Abteilung Strukturchemie, Technische Universität Wien, Getreidemarkt 9/164 SC, 1060 Wien, Austria

[§]Heliatek GmbH, Treidlerstrasse 3, 01139 Dresden, Germany

[∥]Institut für Angewandte Photophysik, TU Dresden, George-Bähr-Strasse 1, 01062 Dresden, Germany

S *Supporting Information*

ABSTRACT: The novel methyl-substituted dicyanovinyl-capped quinquethiophenes **1−3** led to highly efficient organic solar cells with power conversion efficiencies of 4.8−6.9%. X-ray analysis of single crystals and evaporated neat and blend films gave insights into the packing and morphological behavior of the novel compounds that rationalized their improved photovoltaic performance.

Organic solar cell (OSC) research is currently undergoing dynamic development due to its great promise for the production of low-cost and flexible large-area modules as renewable energy sources.[1] In OSCs, conversion of sunlight to electrical energy is realized by the use of synthetic molecular materials, organic electron donors (D) and acceptors (A), as active components.[2] Typically, in solution-processed bulk-heterojunction (BHJ) solar cells, a nanophase-separated blend of a semiconducting polymer as the donor and a soluble fullerene derivative as the acceptor is formed, affording power conversion efficiencies (PCEs) exceeding 8%.[3] More recently, *small-molecule organic solar cells (SMOSCs)* made from conjugated oligomers or dyes have been gaining increasing attention.[4] In this respect, a D−A−D oligomer in combination with a C_{70}-based fullerene acceptor reached a PCE of 6.7% for a solution-processed single-heterojunction (SHJ) device.[5] In vacuum-processed devices, an efficiency of 6.4% was reported for a D−A dye and C_{70}.[6] Stacking of single-junction cells on top of each other allows the construction of tandem cells via vacuum deposition, and this recently led to a certified PCE of 10.7% on an active area of 1.1 cm^2, as disclosed by Heliatek.[7] In comparison to polymeric materials, small molecules and oligomers have the distinct advantages of straightforward synthesis and purification leading to defined molecular structures, which greatly improve the fabrication reproducibility and avoid batch-to-batch variations.

Here we report the synthesis, characterization, and photovoltaic (PV) properties of a novel series of methyl-substituted dicyanovinyl (DCV)-capped A−D−A quinquethiophenes (DCV5T-Me's) **1−3** (Chart 1). Within this series, the methyl substitution pattern along the conjugated backbone was systematically varied, leading to improved efficiencies of 4.8−6.1% in SHJ SMOSCs relative to alkyl-free DCV5T (4.6%; see Table 2) and other alkylated derivatives.[8] Further optimization of the processing parameters during device fabrication using **3** afforded a highest PCE of 6.9%. X-ray analysis of single crystals and evaporated neat and blend layers gave further insight into the packing and morphological behavior of the novel oligomers that rationalized the improved PV performance.

Chart 1. Molecular Structures of DCV5T-Me Donors 1−3

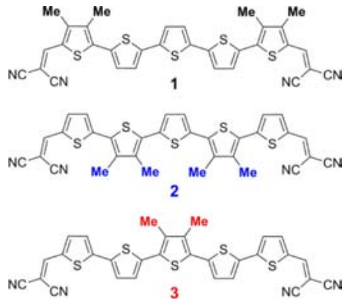

DCV5T-Me's **1−3** were prepared according to a method that had previously been successfully applied in the synthesis of a series of alkyl-free DCV*n*Ts.[8] In the final synthetic steps leading to the poorly soluble target quinquethiophenes **1−3**, Pd-catalyzed Stille-type cross-coupling reactions were used. Detailed synthetic procedures and characterization of **1−3** can be found in the Supporting Information (SI).

For vacuum-processed SMOSCs, thermal stability of the components is essential. The thermal properties of **1−3** were investigated using differential scanning calorimetry (DSC) (Figure S1 in the SI) and thermogravimetric analysis (TGA) (Figure S2). Relative to the parent DCV5T (287 °C),[8] methylation increased the melting point to 301 °C for **3** and 302 °C for **2**, with a further increase to 368 °C for **1**, indicating additional intermolecular interactions in the solid state. For all three derivatives, thermal degradation started at 370−380 °C, as confirmed by DSC and TGA.

Received: March 19, 2012
Published: June 14, 2012

dx.doi.org/10.1021/ja302320c | *J. Am. Chem. Soc.* 2012, 134, 11064−11067

Single crystals of **3** were obtained from gradient sublimation, allowing X-ray structure analysis, which provided information about the molecular geometry and the packing behavior. The thiophene units in **3** show an all-trans conformation, with the DCV groups oriented syn to the S atoms of the terminal thiophenes. The unit cell contains four molecules, and the molecular packing is shown in Figure 1. The molecules are arranged in rows interacting via remarkable H-bonds[9] between vinylic or aromatic CH and the N atom of a neighboring cyano group (C**H**···**N**C = 2.55 or 2.71 Å; blue lines in Figure 1a). The side view reveals that these rows are offset and interact with one another via additional aromatic-C**H**···**N**C short contacts (2.59 Å; red lines in Figure 1a,b). The molecules in the rows stack via $\pi-\pi$ interactions with short contacts as close as 3.28 Å (gray lines in Figure 1b). Important methyl-**H**···**S** dipolar interactions further stabilize the close π-stacking (green lines in Figure 1c). These features, which indicate orbital overlap not only in the stack direction but also perpendicular to the π-stacks, were also found for methylated DCV-capped quaterthiophenes and terthiophenes.[10] In summary, the oligomers are organized in the crystal such that one molecule of **3** interacts with 10 neighboring molecules via 16 well-defined interactions.

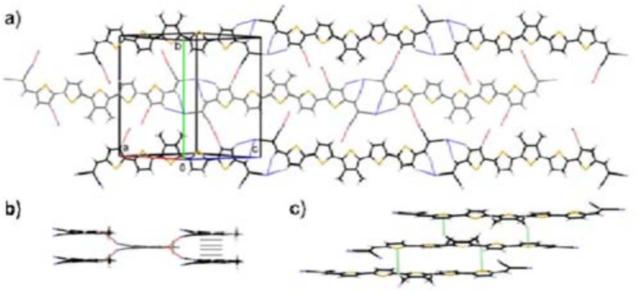

Figure 1. Packing of **3** in a single crystal viewed perpendicular to the (a) (604), (b) (60$\overline{7}$), and (c) (1 10 0) planes of the unit cell.

Figure 2 shows the absorption spectra of **1−3** in solution and in thin films prepared by vacuum deposition (Table 1). In solution, the location and shape of the bands were quite similar for all three derivatives, and the absorption maximum varied from 514 to 527 nm. In the thin films, **1−3** exhibited red-shifted absorption maxima relative to the solution spectra ($\Delta\lambda$ = 50−72 nm), suggesting planarization of the molecules. Within this series and compared with the previously reported alkyl-free[8] and ethyl- or butyl-substituted DCV5Ts,[11] dimethyl derivative **3** showed the most significant red shift of λ_{max} and a more pronounced shoulder at 660 nm, which may indicate better ordering of the molecules in the bulk. The optical gaps for the thin films, as determined from the absorption onsets, were ~1.7 eV, which is ~0.3 eV lower than for the solution spectra.

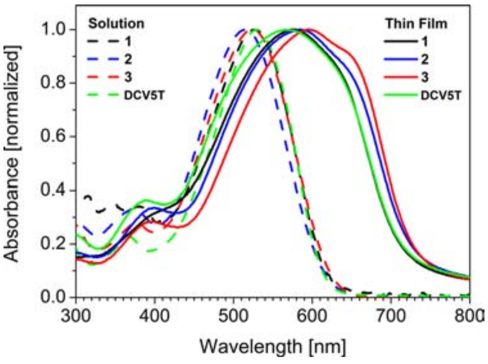

Figure 2. Absorption spectra of **1−3** and DCV5T in CH_2Cl_2 solution (dashed lines) and 30 nm thick thin films (solid lines).

The redox properties of **1−3** were measured in tetrachloroethane/Bu_4NPF_6 solutions at 80 °C (Table 1 and Figure S3). The first oxidation and reduction potentials as well as the band gaps and the calculated HOMO and LUMO energies are very similar for all three pentamers. The relatively low HOMO energies ($E_{HOMO} \approx -5.64$ eV) are expected to result in high open-circuit voltages (V_{OC}) when C_{60} is used as acceptor in OSCs. Also, the LUMO energies ($E_{LUMO} \approx -3.73$ eV) lie in an ideal regime relative to the LUMO of C_{60} (−4.1 eV),[12] which should provide a sufficiently large driving force for charge separation at the D−A interface.

BHJ SMOSCs with a p−i−n-type device architecture[13] were prepared by vacuum deposition of **1−3** as the donor and C_{60} as the acceptor. The layer sequence in the device (stack A) consisted of ITO/C_{60} (15 nm)/donor:C_{60} (30 nm, 2:1 v/v, coevaporated at 90 °C substrate temperature)[14]/BPAPF (5 nm)/BPAPF:NDP9 (50 nm, 90:10 w/w)/NDP9 (1 nm)/Au (50 nm) (see Figure S4). The triarylamine BPAPF p-doped with 10 wt % NDP9 was used as the hole transport layer, on top of which another 1 nm thick layer of NDP9 was deposited to facilitate charge extraction. The active area of each cell was ~6.6 mm^2, as confirmed by comparing short-circuit currents with and without an aperture mask.

The *J−V* characteristics of the stack-A solar cells are shown in Figure 3a and Table 2. The corresponding external quantum efficiency (EQE) spectra are depicted in Figure 3b. All of the solar cells showed high V_{OC}'s above 0.9 V. These values are due to the low-lying HOMOs and are similar to those for other DCV5T derivatives.[8,11a,c] Devices prepared with **1** and **2** turned out to be very similar in terms of short-circuit current density (J_{SC}) (9.6 and 9.4 mA cm^{-2}), fill factor (FF) (63 and 62%), and EQE spectrum (maximum at ~600 nm). Consequently, both **1**- and **2**-based solar cells reached similar PCEs of 4.8%. These reasonable values indicate that excitons are efficiently separated at the D−A interface and readily transported through the bulk. The high saturation [defined as $J(-1\ \mathrm{V})/J_{SC}$], indicating a weak voltage bias dependence of the current in the reverse direction, supports this explanation. The PV performance was further enhanced for devices based on **3**:C_{60}, which showed notably larger values of both J_{SC} (11.1 mA cm^{-2}) and FF (66%) due to efficient charge-carrier extraction, leading to an increased PCE of 6.1%. The superior PV performance of **3** is correlated to the EQE spectrum (Figure 3b), which shows a significant red shift and spectral broadening as in the thin-film UV−vis spectrum.

Because of the outstanding performance of **3**, we further optimized the device stack and processing parameters, resulting in the following layer sequence (stack B): ITO/C_{60}:$W_2(hpp)_4$ (5 nm, 96:4 w/w)/C_{60} (15 nm)/donor:C_{60} (30 nm, 2:1 v/v, coevaporated at 75 °C substrate temperature)/BPAPF (5 nm)/BPAPF:NDP9 (50 nm, 90:10 w/w)/NDP9 (2 nm)/Al (100 nm) (see Figure S4). Stack B differs from stack A in that the substrate temperature was reduced to 75 °C, a 5 nm C_{60} layer n-doped with 4 wt % $W_2(hpp)_4$ was introduced between the ITO and the intrinsic C_{60} layer, the thickness of the p-dopant layer below the top contact was increased, and Au was replaced by Al as the top electrode material. This led to an observed increase in J_{sc} resulting from a significant reduction of electrode

Table 1. Optoelectronic Properties of 1−3 in Comparison with the Parent Compound DCV5T

oligomer	λ_{max}^{abs} (nm) soln	ε_{max} (L mol^{-1} cm^{-1}) soln	E_g^{opt} (eV) soln	λ_{max}^{abs} (nm) film	E_g^{opt} (eV) film	E°_{ox1} (V) soln	E°_{red} (V) soln	E_g^{CV} (eV) soln	E_{HOMO} (eV)[b]	E_{LUMO} (eV)[b]
1	527	–[a]	2.01	577	1.72	0.63	−1.53	1.91	−5.64	−3.73
2	514	60600	2.03	585	1.69	0.60	−1.56	1.90	−5.61	−3.71
3	524	63300	1.99	596	1.69	0.65	−1.50	1.91	−5.66	−3.75
DCV5T	530	73300	2.02	570	1.69	0.64	−1.51, −1.37[c]	1.89	−5.62	−3.73

[a] Molar absorption coefficient could not be determined because of the poor solubility of **1** in organic solvents. [b] Calculated from the onset of the respective redox waves; Fc/Fc$^+$ was set to −5.1 eV vs vacuum. [c] Values determined by differential pulse voltammetry.

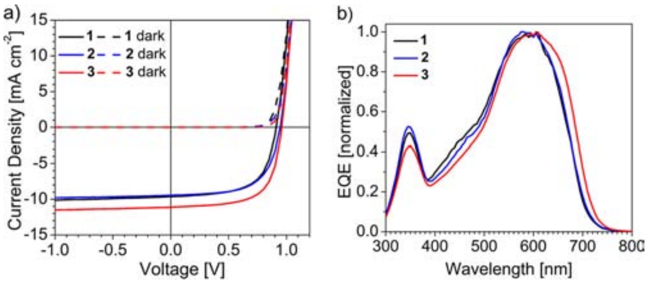

Figure 3. (a) *J*−*V* characteristics and (b) EQE spectra of BHJ solar cells containing oligomers **1−3**. The EQE spectra were used to calculate the mismatch factor for determining the illumination intensity for the measured *J*−*V* characteristics.

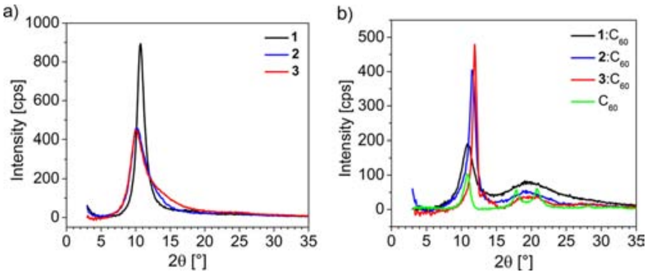

Figure 4. GIXRD patterns of (a) 50 nm films of neat **1−3** deposited on glass substrates at room temperature and (b) 75 nm **1−3**:C$_{60}$ (2:1 v/v) blend layers fabricated by coevaporation on glass substrates at 90 °C, with the pattern for pristine C$_{60}$ shown for comparison.

absorption and an increase in the back-contact reflectance. Optical simulations and a comparison of the EQE spectra of stack-A and -B devices containing **3** showed increased absorption between 400 and 550 nm. The calculated ratio of the absorbed photon flux in the active layer matched the J_{sc} ratio for stacks A and B (see the SI).

We prepared 32 identical solar cells on eight different substrates, which were characterized and statistically evaluated. The devices showed a mean J_{SC} of 11.4 ± 0.09 mA cm^{-2}, V_{OC} of 0.95 ± 0.008 V, and FF of 62.6 ± 0.7%, giving an excellent average PCE of 6.78 ± 0.07% (Table S1 in the SI). These very small standard deviations underline the reproducibility and reliability of our results. The best-performing device generated an exceptional PCE of 6.9% with a V_{OC} of 0.95 V, J_{SC} of 11.5 mA cm^{-2}, and FF of 63% (Figure S5).

To gain deeper insight into the morphological behavior of the novel compounds in thin films, grazing-incidence X-ray diffraction (GIXRD) and X-ray reflection (XRR) measurements on evaporated films (50 nm) of neat **1−3** and blend layers with C$_{60}$ (75 nm) were carried out (Table 2). The GIXRD patterns of the neat films showed an increasing amount of disorder in going from **1** to **3**: while the diffraction pattern of **1** was symmetric, those of **2** and **3** were asymmetric and strongly broadened, indicating smaller domains of ordered areas (Figure 4a). This finding was further corroborated by XRR, which revealed very smooth film surfaces (Figure S6a). To give a rough estimate of the crystal size, the full width at half-maximum (FWHM) was estimated and used in the Scherrer equation with consideration of the instrumental broadening of the GIXRD measurement (this was controlled by a previous Rietveld analysis of test samples). Analysis of the crystal size (lower limit) gave similar values for **2** and **3** (7 ± 2 and 6 ± 2 nm), whereas **1** formed larger crystallites (19 ± 5 nm), in accordance with the trend in the melting points (see above).

In contrast to the neat films, GIXRD of **1−3**:C$_{60}$ blend layers (Figure 4b) surprisingly showed the lowest crystallinity for **1** (7 ± 2 nm), while **2** and **3** exhibited larger crystal sizes of 26 ± 10 and >40 nm, respectively (Table 2). Also, the C$_{60}$ crystal size increased in going from **1**:C$_{60}$ (2.5 ± 0.3 nm) to **2**:C$_{60}$ (2.9 ± 0.4 nm) to **3**:C$_{60}$ (4.1 ± 0.8 nm). These results agree with the XRR data, which showed increasing surface roughness of the films in going from **1** to **3** (Figure S6b). To determine the FWHM of the nanocrystalline C$_{60}$ Bragg reflections, the region 2θ = 15−23° was fitted with two Bragg reflections at identical positions, as for the crystalline neat C$_{60}$ layer.

A comparison of the simulated diffraction pattern of the single-crystal phase and the Bragg reflection of oligomer **3** in the heated blend (Figure 4b) showed a mismatch between the two structures. Nevertheless, we assume that the packing of the molecules in the single crystal should be similar to the packing in blended films. This rationale comes from the similarities of the film growth of DCV-capped quaterthiophenes, which were

Table 2. PV Parameters of BHJ Solar Cells Containing 1−3 or DCV5T and GIXRD Data for Films of Neat 1−3 and Their Blends with C$_{60}$

oligomer (stack)	V_{OC} (V)	J_{SC} (mA cm^{-2})	FF (%)	PCE (%)	intensity (mW cm^{-2})	J(−1 V)/J_{sc}	crystal size neat (nm)	crystal size blend (nm)
1 (A)	0.91	9.6	63	4.8	115	1.05	19 ± 5	7 ± 2
2 (A)	0.95	9.4	62	4.8	115	1.04	7 ± 2	26 ± 2
3 (A)	0.96	11.1	66	6.1	115	1.04	6 ± 2	>40
3 (B)	**0.95**	**11.5**	**63**	**6.9**	**100**	**1.06**		
DCV5T[a]	0.95	9.0	55	4.6	103	1.10	n.d.[b]	n.d.[b]

[a] Comparable thickness of the active layer (ref 11a). [b] n.d. = not determined.

investigated by X-ray measurements and for which the molecular packing was compared to that in single crystals.[10a]

These findings allow us to correlate the morphology of the blend layers (i.e., the size of crystallites) with the solar cell performance. The bigger size of the single-component crystallites for **3**:C_{60} corresponds to a larger D−A phase separation in the blend. This film morphology provides better percolation pathways for the respective charge carriers, which is reflected in the large current density and FF. We attribute the resulting PCE of 6.9% to the high crystallinity of **3** as well as to the relatively high crystallinity of C_{60} compared with the other samples. The C_{60} crystal size marks the significant morphological difference between the blends of **2** and **3**, resulting in large differences in the PCEs of the solar cells.

It still remains an open question why the **1**:C_{60} system showed the smallest phase separation while the small changes in molecular structure in going from **1** to **3** significantly increased the crystallinity and phase separation in **3**:C_{60}. A delicate balance between the homo- and heterointeractions of the two molecular components in the BHJ occurs during the deposition process, which is very sensitive to the substrate temperature. XRD analysis of the D−A blend films showed that the tendency of both components to form larger homophasic crystallites increases in going from **1** to **3**, strongly suggesting reduced $\pi-\pi$ D−A interactions. We assume that C_{60} interacts with **1**−**3** at the central thiophene unit, reducing the repulsion between C_{60} and the DCV acceptor groups.

In summary, we have reported on a novel series of acceptor-substituted quinquethiophenes, DCV5T-Me's **1**−**3**, in which the positioning of methyl substitutents along the conjugated backbone was systematically varied. These oligomers were incorporated into vacuum-processed p−i−n-type BHJ solar cells, which exhibited PCEs of 4.8−6.1%. Through optimization of the processing and fabrication conditions to obtain the best-performing oligomer **3**-based device, the PCE was enhanced to 6.9%, which is the highest reported to date for SMOSCs. XRD measurements of coevaporated D−A films allowed us to correlate the device performance with the morphology of the photoactive blend layer. Single-crystal X-ray structure analysis of oligomer **3** gave deeper insight into the specific intermolecular interactions and multiple nonbonding short contacts, which are responsible for the layer structure with strong $\pi-\pi$ overlap and multidirectional electronic coupling. Finally, our investigations clearly showed that methyl substitution in oligothiophenes can be used to provide a beneficial influence on the morphology of D−A blends and consequently the device performance. This work emphasizes the advantages of structurally defined oligomers, which provide structure−property relationships (molecular level) as well as information on favorable molecular organization in the bulk (supramolecular level) and pronounced phase separation of the donor and acceptor materials in BHJs (systems level).[15]

■ ASSOCIATED CONTENT

Ⓢ Supporting Information

Experimental procedures, additional results, and a CIF file. This material is available free of charge via the Internet at http://pubs.acs.org. The X-ray data were also deposited with the CCDC (entry 850004).

■ AUTHOR INFORMATION

Corresponding Author

peter.baeuerle@uni-ulm.de

Notes

The authors declare no competing financial interest.

■ ACKNOWLEDGMENTS

This work was supported by the DFG (Priority Program SPP 1355) and BMBF (Programs OPEG 13N9720 and OPA 13N98872). We thank Dr. L. Wilde (Fraunhofer CNT) for the X-ray measurements and Novaled AG for providing NDP9.

■ REFERENCES

(1) Brabec, C.; Gowrisanker, S.; Halls, J. M. M.; Laird, D.; Jia, S. J.; Williams, S. P. *Adv. Mater.* **2010**, *22*, 3839.

(2) *Organic Photovoltaics: Materials, Device Physics, and Manufacturing Technologies*; Brabec, C., Dyakonov, V., Scherf, U., Eds.; Wiley-VCH: Weinheim, Germany, 2008.

(3) Dou, L.; You, J.; Yang, J.; Chen, C.-C.; He, Y.; Murase, S.; Moriarty, T.; Emery, K.; Li, G.; Yang, Y. *Nat. Photonics* **2012**, *6*, 180.

(4) Mishra, A.; Bäuerle, P. *Angew. Chem., Int. Ed.* **2012**, *51*, 2020.

(5) Sun, Y.; Welch, G. C.; Leong, W. L.; Takacs, C. T.; Bazan, G. C.; Heeger, A. J. *Nat. Mater.* **2012**, *11*, 44.

(6) Chiu, S.-W.; Lin, L.-Y.; Lin, H.-W.; Liu, Y.-H.; Huang, Z.-Y.; Lin, Y.-T.; Lin, F.; Chen, Y.-H.; Wong, K.-T. *Chem. Commun.* **2012**, *48*, 1857.

(7) Heliatek GmbH, press release of April 27, 2012 (http://www.heliatek.com).

(8) Fitzner, R.; Reinold, E.; Mishra, A.; Mena-Osteritz, E.; Ziehlke, H.; Körner, C.; Leo, K.; Riede, M.; Weil, M.; Tsaryova, O.; Weiß, A.; Uhrich, C.; Pfeiffer, M.; Bäuerle, P. *Adv. Funct. Mater.* **2011**, *21*, 897.

(9) Desiraju, G. R.; Steiner, T. *The Weak Hydrogen Bond*; Oxford University Press: New York, 1999.

(10) (a) Fitzner, R.; Elschner, C.; Weil, M.; Uhrich, C.; Körner, C.; Riede, M.; Leo, K.; Pfeiffer, M.; Reinold, E.; Mena-Osteritz, E.; Bäuerle, P. *Adv. Mater.* **2012**, *24*, 675. (b) Schrader, M.; Fitzner, R.; Hein, M.; Elschner, C.; Baumeier, B.; Riede, M.; Leo, K.; Bäuerle, P.; Andrienko, D. *J. Am. Chem. Soc.* **2012**, *134*, 6052−6056.

(11) (a) Schulze, K.; Uhrich, C.; Schüppel, R.; Leo, K.; Pfeiffer, M.; Brier, E.; Reinold, E.; Bäuerle, P. *Adv. Mater.* **2006**, *18*, 2872. (b) Schulze, K.; Riede, M.; Brier, E.; Reinold, E.; Bäuerle, P.; Leo, K. *J. Appl. Phys.* **2008**, *104*, No. 074511. (c) Mishra, A.; Uhrich, C.; Reinold, E.; Pfeiffer, M.; Bäuerle, P. *Adv. Energy Mater.* **2011**, *1*, 265.

(12) Xie, Q.; Arias, F.; Echegoyen, L. *J. Am. Chem. Soc.* **1993**, *115*, 9818.

(13) Riede, M.; Mueller, T.; Tress, W.; Schueppel, R.; Leo, K. *Nanotechnology* **2008**, *19*, No. 424001.

(14) Wynands, D.; Levichkova, M.; Leo, K.; Uhrich, C.; Schwartz, G.; Hildebrandt, D.; Pfeiffer, M.; Riede, M. *Appl. Phys. Lett.* **2010**, *97*, No. 073503.

(15) Würthner, F.; Meerholz, K. *Chem.—Eur. J.* **2010**, *16*, 9366.